Available online at www.sciencedirect.com
ScienceDirect
Journal of the European Ceramic Society 31 (2011) 2943–2955
www.elsevier.com/locate/jeurceramsoc

Bottom-up and new compaction processes: A way to tunable properties of nanostructured cobalt ferrite ceramics

S. Imine [a,b], F. Schoenstein [a,*], S. Mercone [a], M. Zaghrioui [c], N. Bettahar [b], N. Jouini [a]

[a] Université Paris 13, Pres Sorbonne - Paris-Cité, Laboratoire des Sciences des Procédés et des Matériaux, UPR 3407, CNRS, 99 Avenue J.B. Clément, 93430 Villetaneuse, France

[b] Université des Sciences et de la Technologie d'Oran-MB, Laboratoire de physico-chimie des matériaux, département de chimie, Faculté des sciences, USTO-MB, M'Nouar 1505, Oran 31000, Algeria

[c] Université François Rabelais, Laboratoire d'Electromagnétique des Matériaux Avancés, UMR 6157 CNRS – CEA, UFR Sciences et Techniques, Parc de Grandmont, 37 000 Tours, France

Received 22 November 2010; received in revised form 1 May 2011; accepted 7 June 2011
Available online 16 July 2011

Abstract

In this work we describe a novel bottom-up strategy to process cobalt ferrite $CoFe_2O_4$ nanostructured bulk material. This strategy offers the possibility to drive their magnetic and mechanical properties in a wide range of different behaviors. In particular, we show how to tune the blocking temperature along with optimized mechanical strength. This method combines forced hydrolysis in polyol, a soft chemistry route, and Spark Plasma Sintering (SPS) for consolidation. To highlight this method, we also performed compaction by a standard Hot Isostatic Pressing (HIP) process. Thus we compare the nanostructured bulk microstructures (for both compaction techniques) and magnetic static properties to those of several $CoFe_2O_4$ nanopowder samples showing particle size and annealing temperatures comparable to those of the nanostructured bulk samples. Microstructure, radio-crystallographic and magnetic studies have been carried out in order to show the optimization of the processing strategy in this work.

Keywords: Hot Isostatic Pressing; Spark Plasma Sintering; Spinels; Magnetic properties; Mechanical properties

1. Introduction

Bulk nanostructured materials have been the subject of intense investigations over the last decades[1] due to the unusual properties and their promising applications.[2] Two main classes of nanostructured materials are involved: metals and oxides. Techniques to obtain them involve several methods depending on the compound chosen and on properties required. Nevertheless, we can identify two main strategies to process them: the so-called "top-down" technique and "bottom-up" one. The first one involves a structural disintegration process such as Severe Plastic Deformation (SPD) methods[3] and high energy ball milling.[4] The bottom-up strategy is based on either a one-step processing method such as electrodeposition (ED) or a two-step processing approach in which the synthesis of nanoparticles is followed by consolidation. It is interesting to note that the main methods used to synthesize nanoparticles by the bottom-up strategy, are either physical or electrochemical and that they generally lead to porosity-free samples.[5] Because of their brittle character, bulk nanostructured oxides are mainly processed using the "bottom-up" method.

To obtain improved nanostructured materials using a two-step process, we need to control, during the consolidation step: (i) grain growth[6,7] and (ii) porosity. In order to maintain the properties resulting from the crystallite and/or particle nano-size of the powders in the bulk nanostructured system the first point is necessary. The second is important in order to obtain acceptable mechanical behavior.

In this context, the emerging Spark Plasma Sintering (SPS) method appears to be very promising. In this method, uniaxial pressure and a high pulsed DC current are directly applied to the graphite die containing the powder and so the consolidation occurs in a relatively short time which enables the crystallite and/or the nanoparticle growth to be controlled. This

* Corresponding author at: Tel.: +33 1 49 40 34 95; fax: +33 1 49 40 39 38.
E-mail address: frederic.schoenstein@univ-paris13.fr (F. Schoenstein).

0955-2219/$ – see front matter © 2011 Elsevier Ltd. All rights reserved.
doi:10.1016/j.jeurceramsoc.2011.06.004

emerging consolidation method has been extensively used in the past decades to process dense nanostructured oxide ceramics, such as alumina, magnesium oxide and YAG garnet systems.[8] It has seldom been used for magnetic materials such as cobalt spinel ferrite[9] on which we are focusing-on in this work.

The cobalt ferrite $CoFe_2O_4$ nanoscaled system has been intensively investigated in the last decades thanks to the particle magnetic[10–17] properties it shows, i.e. strong anisotropy, high saturation magnetization, high coercivity field and superparamagnetic character with a blocking temperature approaching room temperature. Even more, these properties usually go along with appreciable mechanical hardness and chemical stability. Thus this system is believed to be useful for several applications such as magnetic storage, optical devices[18,19] and medical applications such as local hyperthermia at cancer sites.[20] Most of these applications obviously need bulk material which possess nanoscaled properties.

Thus the aim of this work is to propose a novel bottom-up strategy to process cobalt ferrite nanostructured material, offering the possibility to drive their magnetic properties in keeping with the applications we aim at. In particular, we show that the magnetic properties due the nanometric size of the particles can be kept at high temperature along with appreciable mechanical strength. This novel bottom-up method combines forced hydrolysis in polyol, a soft chemistry route,[21] and Spark Plasma Sintering way for consolidation. In order to highlight the advantages of this bottom-up method, we compared it with a standard Hot Isostatic Pressing consolidation method. The properties of the as-processed bulk nanostructured samples have also been compared to those of the corresponding $CoFe_2O_4$ nanopowders obtained at different annealing temperatures. Furthermore the magnetic static properties of all our systems will be discussed as a function of the microstructure and radio-crystallographic characteristics of the materials obtained.

2. Experimental details

2.1. Nanopowders "soft chemistry" synthesis

$CoFe_2O_4$ nanoparticles have been synthesized by forced hydrolysis in a polyol medium.[17] Ionic salts: iron (III) chloride hexahydrate, cobalt (II) acetate tetrahydrate and anhydrous sodium acetate were dissolved in stochiometric ratio in 1,2-propanediol (1L) and heated while being mechanically stirred. The polyol acts as a solvent for the salt precursor (high permittivity). It allows to carry out hydrolysis reactions at high temperature up to the boiling point of the polyol and it plays the role of crystal growth media due to its supernatant properties.[22] The total metal ion concentration was 0.3 mol L^{-1} and the hydrolysis ratio, defined as $n H_2O/nM$ (where nH_2O stands for the amount of water and nM for the total amount of metal cations) was fixed by the amount of water in the precursor salts. The sodium acetate ratio defined as nNaOAc/nM was set at 3. The mixture was refluxed (at 180 °C) for 6 h under mechanical stirring (220 tr/min). After cooling to room temperature, the nanoparticles were separated from the supernatant by centrifugation, washed three times with ethanol, then only one time by acetone and deionised water. The purity of the powder is controlled by XRD analysis. Then, the ferrite phase was dried in air at 50 °C (samples A). Finally the as-prepared powders have been thermally treated during 6 h at 300 °C under air to remove the remaining adsorbed organic species (samples B).

Table 1
Summary of powder annealing and sintering conditions.

Sample	Annealing	Sintering
Nanopowders		
A	After synthesis	–
B	300 °C/6 h/air	–
C	400 °C/6 h/air	–
D	500 °C/6 h/air	–
E	800 °C/6 h/air	–
Bulk materials		
F	300 °C/6 h/air	SPS: 500 °C/100 MPa/Argon/5 min
G	300 °C/6 h/air	SPS: 600 °C/100 MPa/Argon/5 min
H	300 °C/6 h/air	SPS: 700 °C/100 MPa/Argon/5 min
I	300 °C/6 h/air	HIP: 600 °C/200 MPa/Argon/60 min
J	300 °C/6 h/air	SPS: 500 °C/100 MPa/primary vacuum /5 min

2.2. Nanopowder sintering techniques

The bulk nanostructured materials have been obtained using Spark Plasma Sintering (SPS) and Hot Isostatic Pressing (HIP).

Using the SPS (SPS Syntex society model 515S), we sintered 1 g of sample B. The powder is placed in a graphite matrix 8 mm in diameter between two electrodes under argon flow. Simultaneously, uniaxial pressure and a high pulsed DC current are applied between the two electrodes and thus on the graphite matrix and the powder inside them. The direct current pulsing duty cycle was set at 12 pulses on and 2 pulses off for 3.3 ms each. The sintering process is operated under dynamic vacuum with partial pressure of argon while being heated at a rate of 100 °C/min and under a pressure of about 100 MPa for a temperature range from 500 °C to 700 °C. All samples were kept for 5 min at the sintering temperature of 500 °C (sample F), 600 °C (sample G) and 700 °C (sample H) (Table 1).

The consolidation of 6 g of sample B has been performed by HIP method. In this case we fill with nanopowders a cylindrically shaped stainless steel container (diameter 2 cm) using a hydraulic press. The capsule is then evacuated to extract gases introduced during the previous step. Due to the nanometric character of the particles, the evacuation of gas molecules from the capsule is long and complex. It requires rise to about 120 h of time to reach a vacuum lower than 10^{-3} Pa. Then the container is sealed by soldering and placed in a furnace. At the beginning, pressure is applied to the sample then temperature increases and pressure changes consequently. The powder is consolidated under high pressure up to 200 MPa, which is possible using an inert gas such as argon. This method almost guarantees a high dense material with a fine grain size and eliminates porous regions produced by agglomerates or the burn-out of organic inclusions.[23,24] An important characteristic of the system, here used, is to monitor the change in density during the whole sin-

tering process. The compaction device used in this study had a special expansion cell within the hot press permitting the measurement of the capsule height or width during compaction. This gives information on sample density[25] and determines the temperature and time limit as from which there is a drop in the densification rate in the absence of grain growth. HIP sintering was conducted under a temperature of 600 °C and a pressure varying in the range 150–200 MPa.

In order to study the effect of sintering temperature on the properties of nanostructured bulk materials we also performed sintering of $CoFe_2O_4$ nanopowders in air, at atmosphere pressure for 6 hours at several temperatures 400 °C (sample C), 500 °C (sample D) and 800 °C (sample E).

Powder and compacted powder processing conditions are summarized in Table 1.

2.3. Characterization techniques

Several techniques have been used in order to study the structural and magnetic properties of our samples.

X-ray diffraction (XRD) patterns were recorded at room temperature using an INEL diffractometer equipped with curved position linear detector (cobalt anticathode ($\lambda = 1.7809$ Å)) with 120° of aperture and step of 0.015° between two channels. For the data collection only the range 10–90° was taken into account. The experimental data were collected during an acquisition time of 720 min with precision of ±0.03°. Rietveld standard refinement of the data in order to obtain lattice parameter was performed using the FULLPROF program with a pseudo-Voigt diffraction line profile.[26] Crystallite size and strain were inferred from the broadening of the diffraction peaks using the following well-known Eq. (1) [27]:

$$\beta \cos\theta = \frac{\lambda}{D} + \eta \sin\theta \quad (1)$$

where β is, in radians, the full width at half maximum (FWHM) value of diffracted peaks, θ is the Bragg angle, λ is the wavelength of the X-rays used (Co-$K_{\alpha 1}$ radiation: $\lambda = 1.7809$ Å), D is the crystallite size and η is the strain. The determination of β needs to be made after correction of the instrumental X-Ray pattern estimated by the Cagliotti method using polycrystalline LaB_6 as standard.[28]

Particle morphologies, sizes and nanostructuration of corresponding bulk materials have been studied by MEB-FEG (ZEISS SUPRA 40VP) and by Transmission Electron Microscopy (TEM) using High Resolution Electron Microscope JEOL 2011 (200 kV, resolution 0.19 nm). Thin foils for TEM observations were prepared using a Gatan precision ion polishing system (PIPS), with a current of 0.5 mA and a voltage of 5 kV at starting angles of ±7°. Grain boundaries of approximately 100 grains were depicted manually with the IMAGE TOOL software using TEM bright field images to determine the grain size.

The densities of the nanostructured massive materials were measured by the Archimede method at room temperature by immersing the samples in a xylene medium.

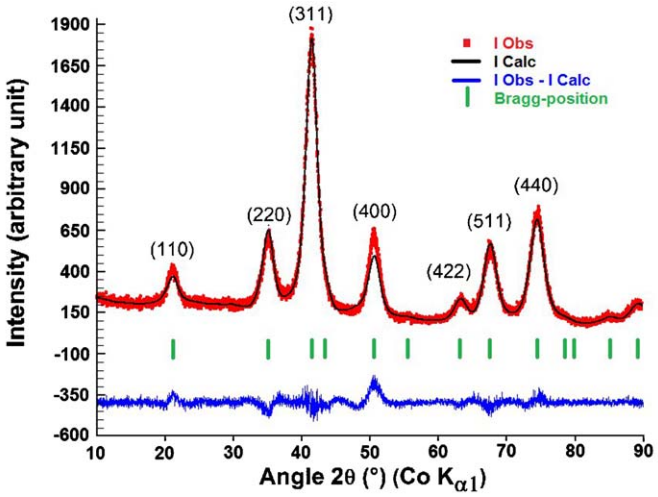

Fig. 1. Rietveld refinement profile of $CoFe_2O_4$ as-obtained powder. Calculated (black line) and measured (red dots) patterns are explained in the up right legend. Bragg reflections positions expected for $Fd\bar{3}m$ space group are indicated with green lines. In the bottom of the graph difference between calculated and observed diffraction intensities is shown (blue line). (For interpretation of the references to colour in this figure legend, the reader is referred to the web version of this article.).

Micro-hardness measurements were conducted on the plane perpendicular to the pressing direction using a Duramin 20 Vickers device under a test force of 1.916 N for 5 s.

The thermal decomposition behavior of the as-synthesized powder was examined by means of thermo-gravimetric analysis (TGA) using a SETSYS Evolution-1750 SETARAM instrument in an argon atmosphere at a heating rate of 10 K min^{-1}.

Magnetic susceptibilities, $\chi(T)$, have been measured with a Manic Faraday-based magnetosusceptometer equipped with a furnace. The data have been collected in zero-field cooling (ZFC) and field cooling (FC) modes in a temperature range from 300 K to 830 K for an applied magnetic field of 450 Oe. For ZFC measurements, samples were heated up to 830 K (higher then the blocking temperature) under zero magnetic field applied and then cooled down to 300 K. After the application of a magnetic field at 300 K, magnetic moments were measured up to 830 K. Then FC measurements were collected when cooling down again. A hysteresis loop, $M(H)$, was carried out using a Physical Property Measurements System (Quantum Design cryostat PPMS 6000) between 80 K and 400 K.

3. Results and discussion

3.1. $CoFe_2O_4$ nanopowders

X-ray powder diffraction patterns of as-elaborated nanopowder (Fig. 1) reveal a $CoFe_2O_4$ single-phase composition (JCPDS Card Number 22-1086). All the peaks observed are well indexed in terms of the cubic symmetry $Fd\bar{3}m$ space group ($a = 8.37$ Å) (due to the very wide diffraction peak, the cell parameter cannot be precisely calculated, here we give an estimated value). The cell parameter was also inferred from the Poix relation (2) giving the cell parameter as a function of the

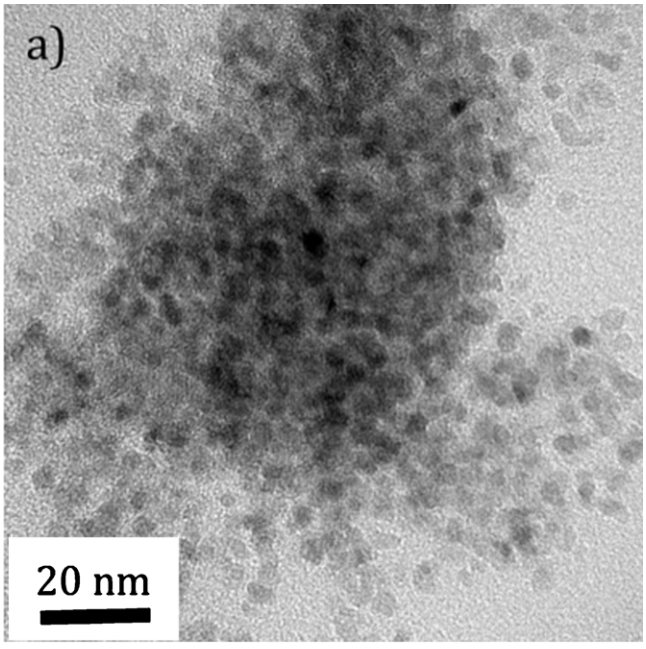

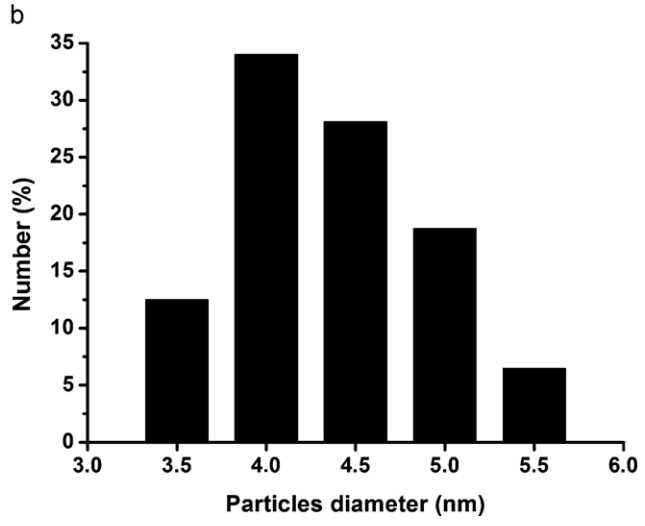

Fig. 2. (a) TEM image of $CoFe_2O_4$ as- grown nanoparticles, (b) $CoFe_2O_4$ nanocrystal size histograms distribution measured by TEM micrographs.

cation–anion distances in both tetrahedral (d_{Td}) and octahedral (d_{Oh}) sites of the spinel structure[29,30]

$$a = 2.0995 d_{Td} + \sqrt{5.8182 (d_{Oh})^2 - 1.4107 d_{Td}^2} \quad (2)$$

The cell parameter obtained considering the cation distribution previously reported for such a compound[17]: $(Co_{0.16}Fe_{0.84})[Co_{0.84}Fe_{1.16}]O_4$ is in keeping with that inferred from experimental data (8.384 Å compared to 8.37 Å).

Transmission Electron Microscopy (TEM) (Fig. 2a) shows well-dispersed and homogeneous nanoparticles and makes possible to estimate the distribution of particle size. The latter is centered at 4 nm with a dispersion deviation less than (Fig. 2b). This is pratically in keeping with the X-ray calculations (5 nm) and clearly demonstrates that the as-obtained nanoparticle is a mono-crystallite system.

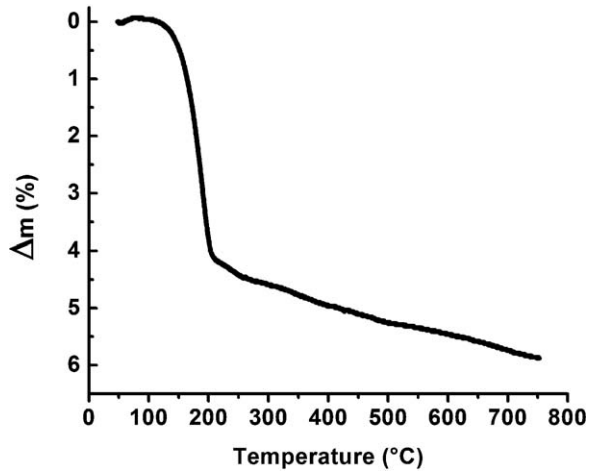

Fig. 3. TG–DT analysis of as-obtained nanopowder.

The TGA curve for the as-obtained powder is shown in Fig. 3. It reveals a weight loss of about 3% occurring at 200 °C that it could be due to the departure organic species such as polyol adsorbed on the surface of nanoparticles in good agreement with previously works dealing with the synthesis of inorganic materials in polyol medium.[31–33]

Fig. 4 shows XRD patterns of nanopowders obtained at different annealing temperature (i.e. samples A–E, see Table 2). All these powders show a $CoFe_2O_4$ single phase, no secondary phase is also detected after annealing. The diffraction peak's width significantly decreases when the annealing temperature is increased. This clearly indicates that the crystallite size increases with increasing annealing temperature.

Fig. 5 clearly shows that the variation of $\beta \cos\theta$ versus $\sin\theta$ is linear for all our samples as expected by Eq. (1). Crystallite size (D) was obtained by extrapolation using Eq. (1). D goes from 6.5 nm to 41 nm as the annealing temperature increases from

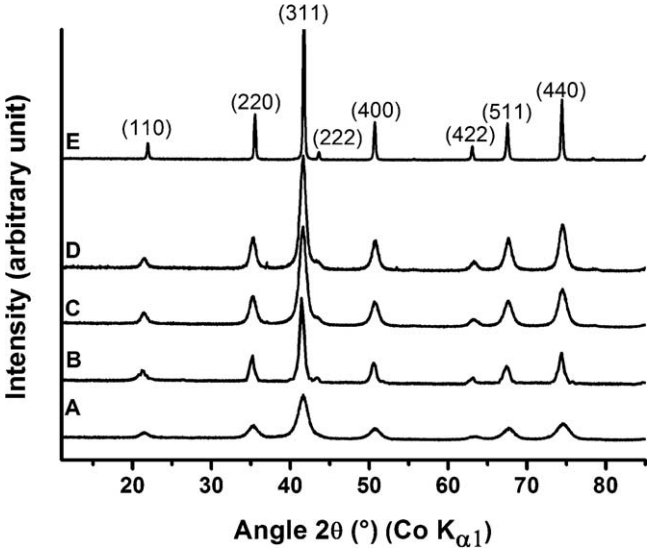

Fig. 4. $CoFe_2O_4$ nanopowders X-ray diffractograms of sample A: after synthesis, sample B: after annealing at 300 °C, sample C: after annealing at 400 °C, sample D: after annealing at 500 °C and sample E: after annealing at 800 °C.

Table 2
Summary of structural properties of as-obtained and annealed powders and sintered nanostructured materials studied by X-ray diffraction and TEM images.

Sample	Lattice parameter "a" (Å)	Apparent density (g/cm^3)	Relative density (%)	Crystallite size Φ_{XRD} (nm) (Williamson and Hall)	Particle size: Φ_{MET} (nm)
Nanopowders					
A	8.37[a]	–	–	5.0 (2)	4–5
B	8.33[a]	–	–	6.5 (2)	10–12
C	8.346(3)	–	–	9.5 (5)	12–15
D	8.352(5)	–	–	11.0 (7)	15–20
E	8.346(2)	–	–	41 (9)	40–100
Bulk materials					
F	8.366(4)	4.83(5)	92	11.5(8)	10
G	8.385(4)	4.91(6)	93	13.5(6)	12–15
H	8.378(6)	4.90(9)	93	31(4)	40–50
I	8.394(4)	5.06(3)	96	56(8)	0.2–2 μm

[a]This is an estimated value. Due to very large diffraction peaks, the lattice parameter cannot be determined with precision for the powders obtained just after synthesis and after the first annealing.

300 °C to 800 °C (see Table 2). It is interesting to note that all curves present almost identically very small slope values indicating the absence of strain in our particles. Thus the soft chemistry technique used here is the best way to minimize the internal strain of nanoparticles along with an optimized crystallinity in comparison with several other processing methods.[15,16,34]

The morphologies of $CoFe_2O_4$ nanopowders are presented in Fig. 6. The effect of annealing on particle shape and size is clear. The mean particle size determined from recorded TEM micrographs for each sample is referred in Table 2. It increases from 10 to 100 nm as the annealing temperature increases from 300 to 800 °C. The as-obtained $CoFe_2O_4$ "mono-crystal nanoparticles" heated at 300 °C (Fig. 6a) presents almost spherical shape. As the annealing temperature increases, the particle size increases (Fig. 6b). At 800 °C, particles seem to fuse together to form bigger aggregates of larger polycristalline particles [samples D and E] due to the grain growth and aggregation of the particles (Figs. 6c and d). We can also notice that increasing annealing temperature increases the polycrystalline character of nanoparticles.

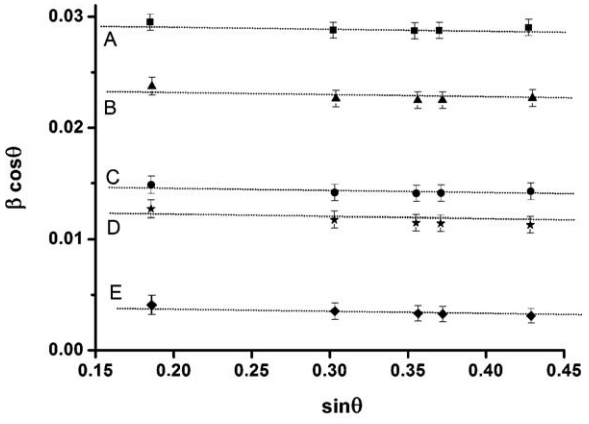

Fig. 5. Strain graphs $\beta \cos\theta$ versus $\sin\theta$ for the $CoFe_2O_4$ nanopowders.

3.2. Bulk nanostructured $CoFe_2O_4$ samples

3.2.1. Sintering

Fig. 7 shows the typical temperature variation and z-axis displacement behavior of the sample during SPS sintering. After reaching its maximum value, the voltage between electrodes starts to decrease (Fig. 7a) and this can be related to the increase of the sample temperature[35] (Fig. 7b). The displacement profile shown in Fig. 7b reveals that the shrinkage of the material begins immediately during the heating cycle as indicated by the rapid z-axis decrease. This first shrinkage observed for temperature between 20 and 300 °C may be attributed to the release of still adsorbed organic species as evidenced by the TGA analysis discussed above. It can also be due to the large large rearrangement of particles due to the temperature and applied pressure actions. The densification effect starts really after 400 °C in the example shown. For the as-processed powder, this effect occurring between 400 and 600 °C seems to be more important. Kodash et al.[36] reported that if the sintered powder presents initially a wide distribution of particle size, this may contribute to the grain growth during sintering. Also, Groza and Dowding[37] reported that non-agglomerated particles sinter at a lower temperature. In our case the as-elaborated $CoFe_2O_4$ particles present either the advantage of non-agglomeration configuration or the monodispersion of size, which is the cause of the limited grain growth and the relatively low sintering temperature observed. The maximum sample displacement is observed during the heating cycle (around 85% of the total displacement) then it remains constant during the dwell sintering and increases during the cooling of the sample due to the thermal expansion effects.

The shrinkage curves recorded during the SPS experiment is reported in Fig. 8. The sintering temperature induces an increase of the final density sample. The bulk densities of the as-sintered samples are slightly lower than the theoretically calculated density (5.274 g/cm^3) (see Table 2). Thus bulk nanostructured material with relative density between 92 and 93% can be obtained within a short sintering time (5 min) using SPS. Moreover the SPS treatment affects in a relatively modest man-

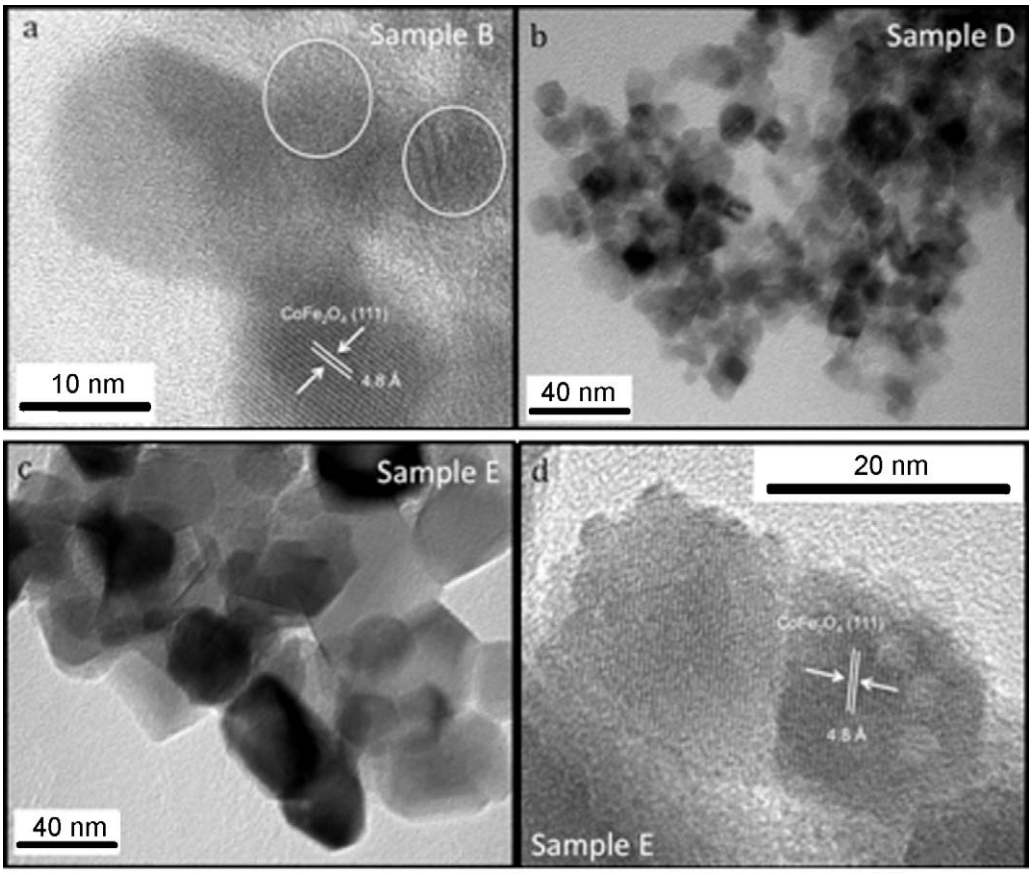

Fig. 6. TEM pictures of nanopowders after different annealing temperatures: (a) sample B calcinated at 300 °C; (b) sample D calcinated at 500 °C and (c and d) sample E calcinated at 800 °C.

ner the $CoFe_2O_4$ grain size, which are maintained between 10 and 35 nm (see Table 2) and this was one of our main goals in the sintering of nanostructured bulk magnetic oxides.

Fig. 9 shows an example of the HIP heating and pressure cycle. A pressure of 150 MPa is initially maintained in the HIP press, in order to slowly increase with the oven temperature. A first step of the powder densification is observed due to this pressure effect. This displacement is then attributed to a cold compaction of the powder. At this stage the temperature increases (375 °C/h) causing an increase in pressure (Fig. 9). As in SPS sintering, 85% of the powder densification takes place during the heating ramp cycle. Finally, the temperature and pressure are maintained at 600 °C and 200 MPa during the dwell sintering (60 min) and we observed a constant z-axis displacement during the holding sintering. This HIP treatment applied to sample B produces an ultra-fine grained material (see Table 2, sample I) with a final relative density of 96%, which it is going to be a useful comparison to previous samples.

3.2.2. *Relative density as a function of the consolidation method and X-ray study*

In order to limit particle growth caused by diffusion during the compaction, we applied relatively low temperature (not exceeding 700 °C) and we limited the applied pressure to 100 MPa when using SPS method and to 200 MPa for HIP method. In these conditions all compacted materials present an apparent density close to the theoretical one (see Table 2: relative density between 92 and 96%). The porosity of each sample is calculated according to the formula (3)[38]:

$$p = \left[\left(1 - \frac{\rho^*}{\rho_s}\right) \times 100\right] \quad (3)$$

where ρ^* is the apparent density of compacted samples and ρ_s the theoretical density of $CoFe_2O_4$ ($g\,cm^{-3}$). Samples G and H present almost identical porosity (7%; Table 2). Sample I obtained by HIP compaction is less porous than by SPS compaction (4%). This may be due to the needs of higher pressure for the HIP compaction.

X-ray diffraction patterns for the nanostructured bulk systems are shown in Fig. 10. A secondary phase namely hematite Fe_2O_3 is observed when SPS experiments are conducted under primary vacuum. Millot et al. also observed a secondary phase namely CoO when SPS sintering is conducted at 1000 °C under vacuum. Lowering the temperature to 800 °C allowed these authors to obtain pure $CoFe_2O_4$.[9] In the present work, we succeeded in processing pure cobalt ferrite phase using dynamic vacuum under argon instead of primary vacuum during SPS compaction. It is also interesting to note that despite the high pressure employed in HIP compaction, a pure $CoFe_2O_4$ phase is observed.

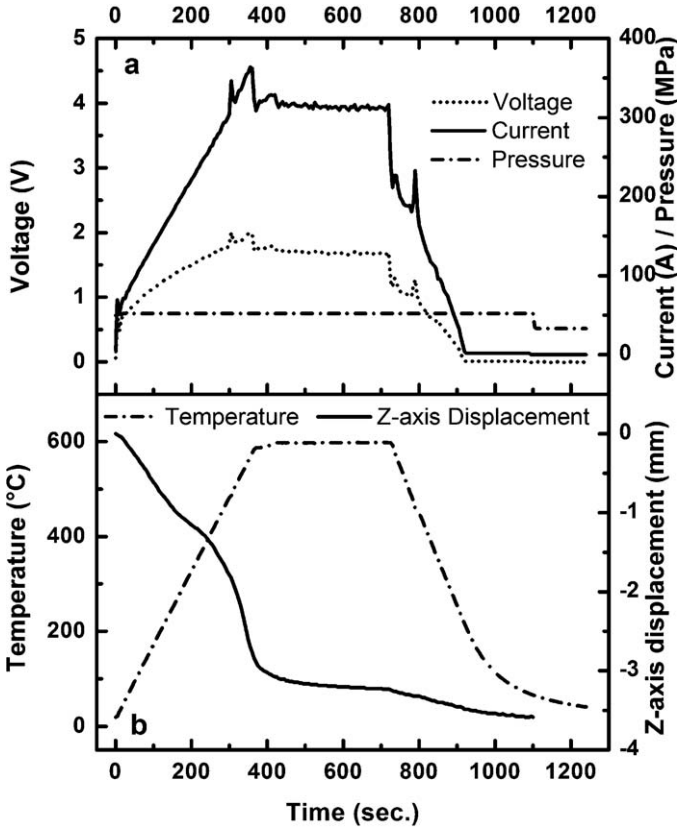

Fig. 7. Typical voltage, current, pressure and temperature variations and z-axis displacement behavior during Spark Plasma Sintering technique. Here we report the example of $CoFe_2O_4$ nanopowders sintered sample at temperature of 600 °C (sample G).

3.3. Temperature effect on the structural properties

In Fig. 11, we report cell parameter variation versus annealing/sintering temperature of our nanopowders and bulk materials. The as-synthesized nanopowders have a lattice parameter of 8.37 Å (Table 2). A decrease in the cell parameter is observed when the as-obtained nanopowder is heated at 300 °C (8.326(2) Å). Further annealing at a higher temperature led the

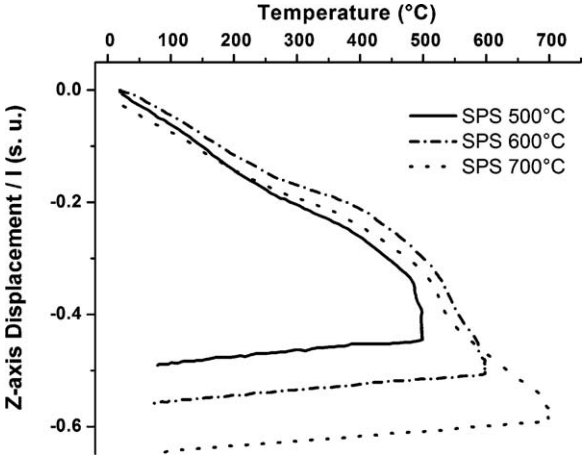

Fig. 8. Shrinkage of the $CoFe_2O_4$ nanopowders sintered systems (sintering temperatures are: 500 °C, 600 °C and 700 °C and sintering time is 5 min).

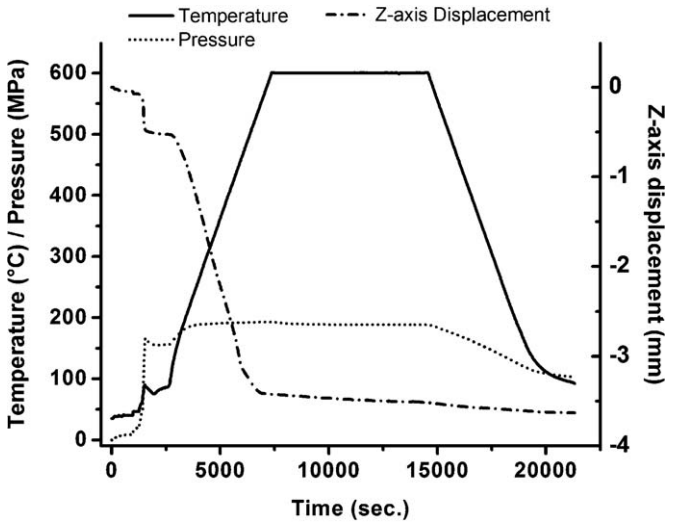

Fig. 9. Typical pressure, temperature and z-axis displacement variations during HIP sintering of $CoFe_2O_4$ nanopowders (sintering temperature is 600 °C and holding time is 60 min).

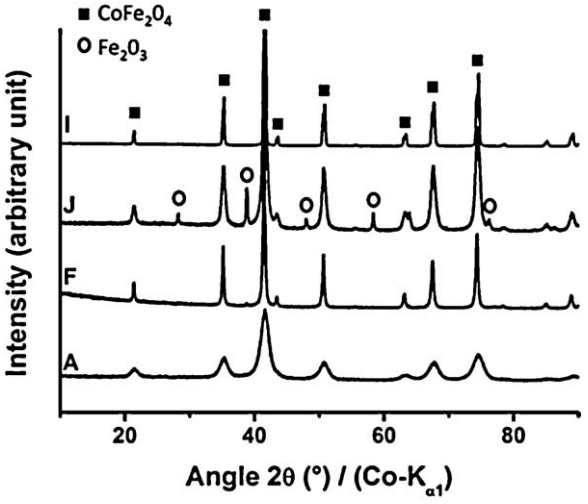

Fig. 10. X-ray diffractograms of $CoFe_2O_4$ samples after sintering by HIP and SPS. Sample A: nanopowders after synthesis; sample F: SPS at 500 °C/100 MPa/Argon/5 min; sample J: SPS: 500 °C/100 MPa/Vacuum/5 min; sample I: HIP at 600 °C/200 MPa/Argon/60 min.

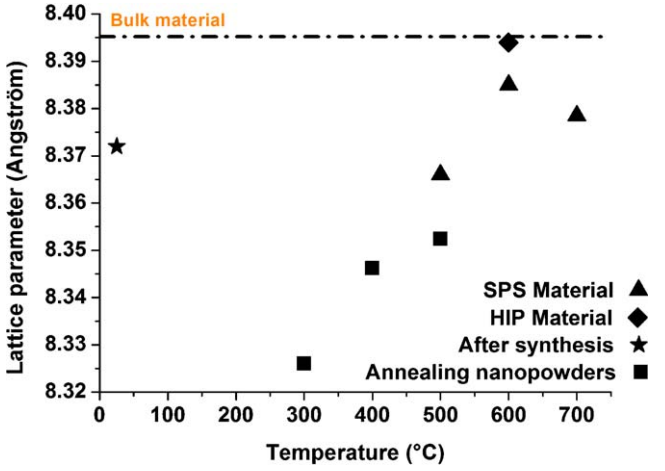

Fig. 11. Lattice parameter variation versus the annealing/sintering temperature.

cell parameter to increase. Both temperature and pressure in SPS and HIP compaction continue to increase the cell parameter of the compacted nanopowder. The cell parameter of the Hipped nanostructured system is close to that of the bulk parameter ($a = 8.395(5)$ Å[39]).

In the case of nanopowder, the evolution of the lattice parameter versus the annealing temperature is similar to that previously reported by Malats I. Riera et al.[40] and Millot et al.[9] The cell parameter obtained in the present work when the sample is annealed at 300 °C is very close to that reported by Malats I. Riera et al. (8.321 Å compared to 8.29 Å). These authors attributed the decrease of the lattice parameter, of the as-prepared sample at 300 °C compared to the as-obtained one, to the oxidation of the cobalt cation Co^{2+} to Co^{3+}. This oxidation is less observed when the sample is heated at a temperature higher than 300 °C. It should be noted that the redistribution of the cations between the two sites may also explain this cell parameter variation. However this hypothesis should be ruled out in our samples since Chinnasamy et al.[41] have shown that the cation distribution sites is size independent for nanoparticles 8 to 100 nm in diameter which is our case (all our samples have a diameter less than 40 nm, see Table 2). Thus oxidation of cobalt cations[9,40] is at the origin of the observed cell parameter variations. Furthermore, using the method of characteristic distances developed by Poix, the amount of Co^{2+} transformed into Co^{3+} was estimated to be about 15%. Indeed the cell parameter calculated in the hypothesis of Co^{3+} located in octahedral sites (8.34 Å) agrees well with the observed one (8.33 Å).

3.4. Microstructures and mechanical behavior

The sample microstructure compacted by SPS and HIP was characterized by TEM imaging (SPS sample) and by SEM-FEG respectively, as shown in Fig. 12. The first clear result is that the two methods induced different microstructural characteristics. The SPS compaction does not significantly change the particle size. Indeed, the samples appear to be made up of grains of homogeneous nanometric size (Fig. 12a: image is representative of all pictures taken on this sample). Even more, if we compare this size to those of the nanopowder particles sintered at the equivalent temperature used for compaction (i.e. sample D, annealing at 500 °C/6 h/air), then we discover that they are equal within the experimental error. In both cases, the nanoparticles/grains appear to be monocrystalline. The higher the sintering temperature, the higher the crystallite size (see Table 2). On the other hand, the HIP compaction induced significant changes (Fig. 12b). The grains morphology becomes polygonal and their sizes reach the micrometric value (0.2–2 μm). However the crystallite size remains in the nanometer range (55 nm) even if this is considerably higher than in the SPS samples.

As we just reported, the grain size of SPS bulks sintered material is smaller than that observed in the HIP sintered sample. This could be related on one hand to the greater pressure applied in the HIP case, which increases the surface activity of the particles and accelerates the dynamic grain growth. On the other hand, the rapid heating rate and the very short dwelling time in the SPS process, both play an important role in the diffusion matter confinement at the surface of the grains.

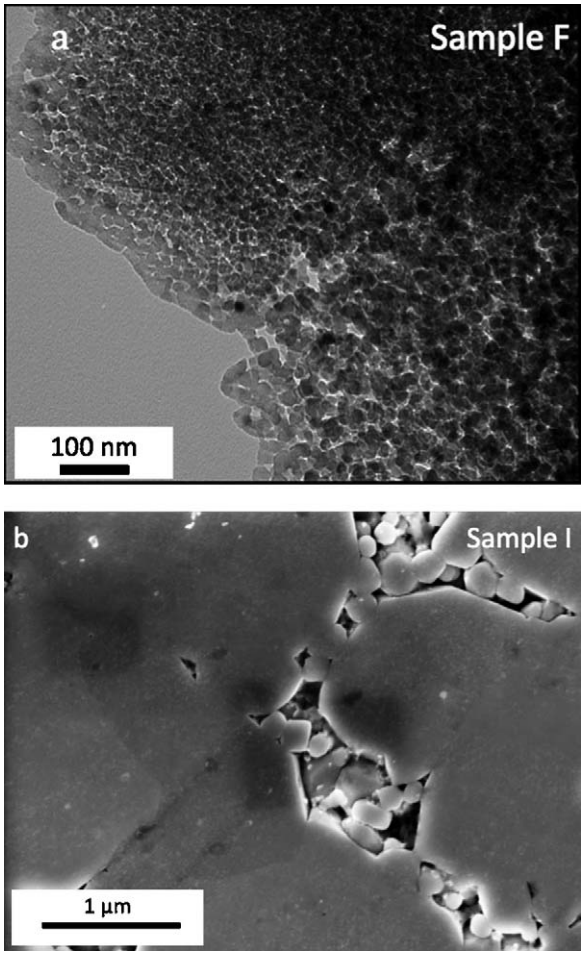

Fig. 12. (a) TEM observation of SPS nanostructured bulk system: sample F – 500 °C/100 MPa/Argon/5 min; (b) SEM-FEG observation of HIP nanostructured bulk material: sample I – 600 °C/200 MPa/Argon/60 min.

Vickers microhardness measurements were realized for all the massive materials (Fig. 13). Those results shown high

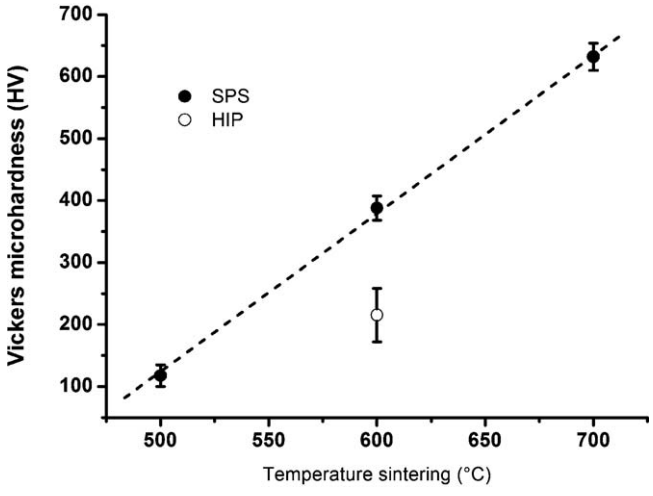

Fig. 13. Vickers microhardness (HV) variation versus the sintering temperature in SPS and HIP compaction methods.

Table 3
Magnetic properties of as-grown powder, annealed and synthesized nanostructured materials.

Sample	Particle size: Φ_{MT} (nm)	Saturation magnetization at 300 K (emu/g)	Coercive field at 300 K (Oe)	ZFC–FC T_{max} (K)	ZFC–FC T_{diff} (K)	Ref.
Nanopowders						
A	4–5	69	10	320	320	[17]
B	10–12	57	140	380	380	This work
C	12–15	61	210	430	480	This work
D	15–20	64	550	440	500	This work
E	40–100	85	835	550	660	This work
Bulk materials						
F	10	51	580	490	600	This work
G	12–15	69	525	520	630	This work
H	40–50	70	660	570	640	This work
I	0.2–2 μm	85	600	650	720	This work

hardness in the SPS compound compared to the HIP compound sintered at the same temperature (600 °C). Regarding the SPS samples, we should note that the Vickers microhardness increases linearly with the sintering temperature as clearly shown by Fig. 13. This can be related to the increase in the density according to temperature. The microhardness obtained at 700 °C (value around 600 HV) is very close to that previously reported for $ZnFe_2O_4$[42] and $MgAl_2O_4$.[43] The interesting result in Fig. 13 is that the SPS compaction process allows us to obtain nanostructured spinel $CoFe_2O_4$ with tunable hardness which varies from that of metal (low hardness) to that of ceramic material (high hardness). This property can simply be driven by adjusting the sintering temperature.

3.5. Magnetic static properties

The main magnetic results are summarized in Table 3.

The saturation magnetization (M_s) has been calculated thanks to the well-known Eq. (4) in the hysteresis loop data at 300 K.

$$M_{MES} = M_s\left(1 - \frac{a}{H}\right) \quad (4)$$

where M_{MES} is the magnetization measured at each magnetic field applied M_s is the saturation magnetization value and H is the applied magnetic field. The as-prepared powder presents a high saturation magnetization (69 emu/g) close to that of the $CoFe_2O_4$ bulk material (80 emu/g), this once again confirms the pure phase of our as-obtained powder and its improved crystallinity. When the powder is calcinated at 300 °C, the saturation magnetization value decreases slightly. This variation is similar to that of the cell parameter and is in keeping with results previously reported by Malats I. Riera et al.[40] who suggested that this diminution can be due to the oxidation of Co^{2+} into Co^{3+} a diamagnetic cation. Then M_s linearly increases following the increasing crystallite size (i.e. increasing annealing temperature) and it again reaches the value of the bulk material for the bulk nanostructured compacted systems (see Tables 2 and 3). Such increase in the magnetization saturation with the annealing temperature has recently been reported for Ni-Zn ferrite nanoparticles annealed at various temperatures up to 600 °C.[44]

The ZFC–FC measurements for all nanopowders and consolidated samples are reported in Figs. 14 and 15 respectively.

A clear irreversible behavior is observed between ZFC and FC magnetization measurements. Indeed, for each sample, there exists a critical temperature above, which the ZFC and FC susceptibilities overlap and decrease as the temperature increases. Below this critical temperature noted T_{diff} (Table 3), the ZFC decreases while FC increases.

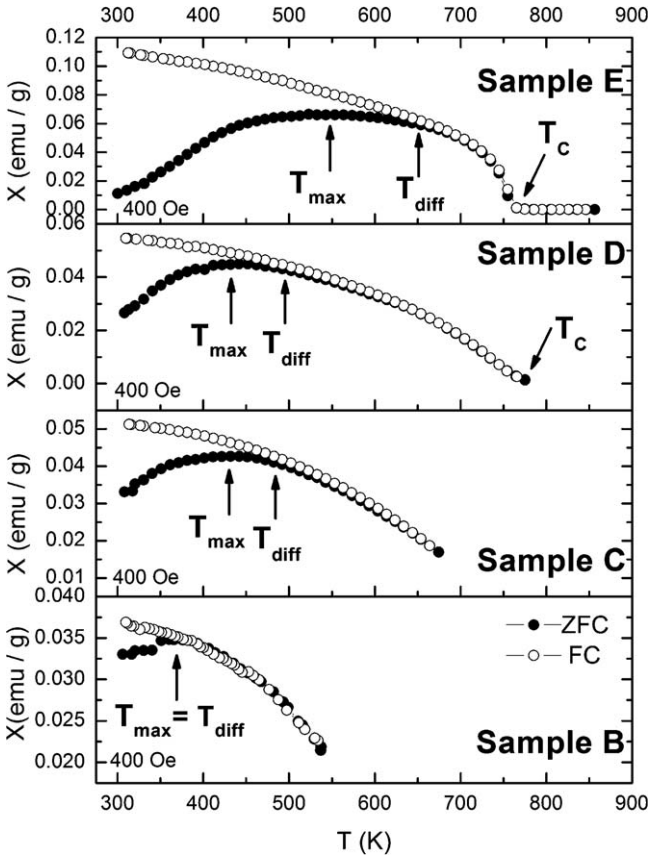

Fig. 14. Temperature dependence of ZFC–FC magnetization measurements of nanopowders annealed at 300 °C (sample B), at 400 °C (sample C), at 500 °C (sample D) and at 800 °C (sample E).

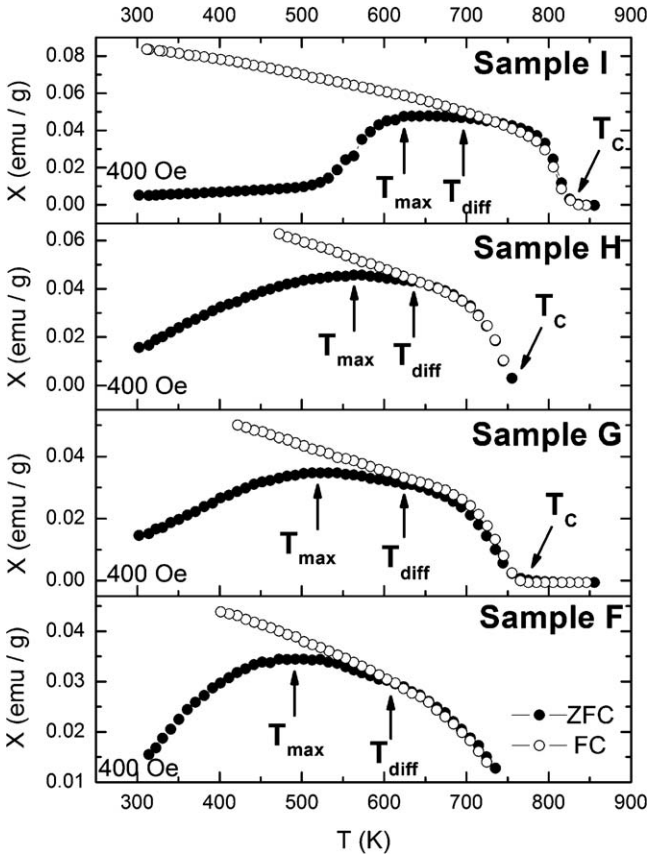

Fig. 15. Temperature dependence of ZFC–FC magnetization measurements of nanopowder sintered by SPS at 500 °C (sample F), at 600 °C (sample G), at 700 °C (sample H) and by HIP at 600 °C (sample I).

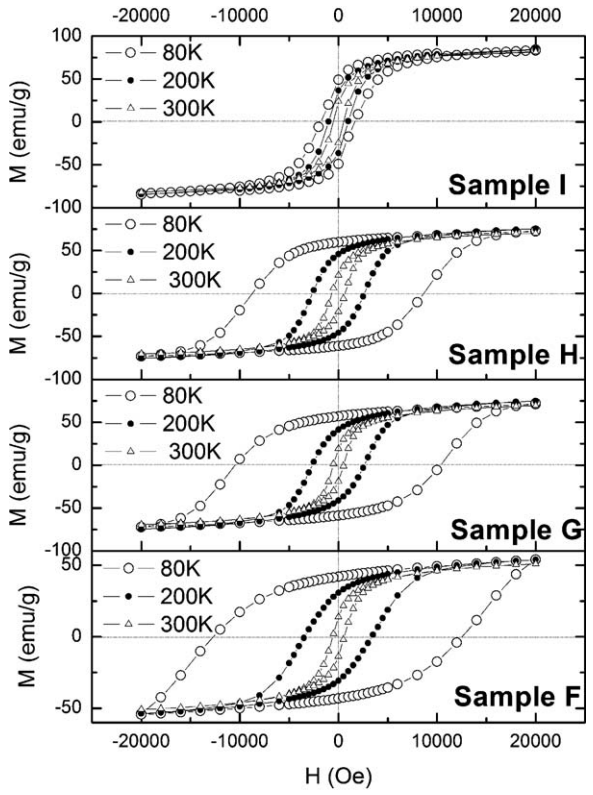

Fig. 16. Magnetization curves for sample F: SPS sintered at 500 °C, sample G: SPS sintered at 600 °C, sample H: SPS sintered at 700 °C and sample I: HIP sintered at 600 °C at 80 K, 200 K and 300 K.

Hysteresis loop magnetization measurements at different temperature as function of the applied magnetic field up to 2.5 T were also performed. As shown in Fig. 16 both nanopowders and consolidated samples present, below the critical temperature T_{diff}, open hysteresis loops with a coercive field (H_c) and high remanent magnetization (M_r). Those hysteresis cycles shrink to zero when T approaches the overcome of the critical temperature T_{diff} value.

All together these characteristics may be due to the existence of the superparamagnetic or ferrimagnetic character of the samples studied. In the first hypothesis T_{diff} will represent the blocking temperature (T_B) while in the second case this temperature will characterize the Curie temperature (T_C). It should be noted that the Curie temperature is usually determined from the minimum of the temperature dependence of M ($M = 0$, $T = T_C$), which corresponds very closely to the onset of the increase in magnetization.[45–47] Taking into account this definition, one can remark looking at Figs. 14 and 15 that T_{diff} cannot correspond to Curie temperature. Indeed as shown in Figs. 14 and 15, the Curie temperature is around 750–800 K close to that of the bulk cobalt ferrite (790 K).[47] This value is in keeping with that recently reported (820 K) by Franco et al. for cobalt ferrite nanoparticles 42 nm in diameter.[48]

Finally the samples studied here can be classified into two sets. Sample E (nanopowder calcined at 800 °C) and sample I (HIP consolidation) present a particle size greater than 40 nm the critical size for cobalt ferrite monodomain particle.[41] For this set, the superparamagnetism character appears to play a minor role. Thus the irreversibility observed in this case between ZFC/FC susceptibilities can mainly originate from the domain wall depinning[32,49] in cobalt ferrite bulk coarsened multi-domain particles rather than from superparamagnetic behavior.

Samples with particle size lower than 40 nm can be considered as superparamagnetic systems (SP) with T_{diff} representing the blocking temperature. It should however be noted that two critical temperatures are generally defined for superparamagnetic nanoparticles T_{diff} at which ZFC and FC curves overlap and T_{max} at which ZFC curve reaches a maximum, the latter being usually taken as the blocking temperature.

The existence of these two critical temperatures is generally associated to the dispersion of the size of superparamagnetic particles.[50] The blocking temperature (T_{max}) is associated with an average size of the particles. The point at which the ZFC–FC curves start to diverge (T_{diff}) is associated with the blocking temperature of the bigger particles. The difference between these two temperatures reflects the distribution in the particle size. This is obviously the case in the systems studied (see Figs. 14 and 15). FC behavior observed below the blocking temperature is generally interpreted as a combination of two main processes[51,52] magnetic particle structure and dipolar interactions between particles. For non-interaction ferromagnetic and/or ferrimagnetic particles, magnetization increases with decreasing temperature ($T <$ blocking temperature). This is obviously not the case in our

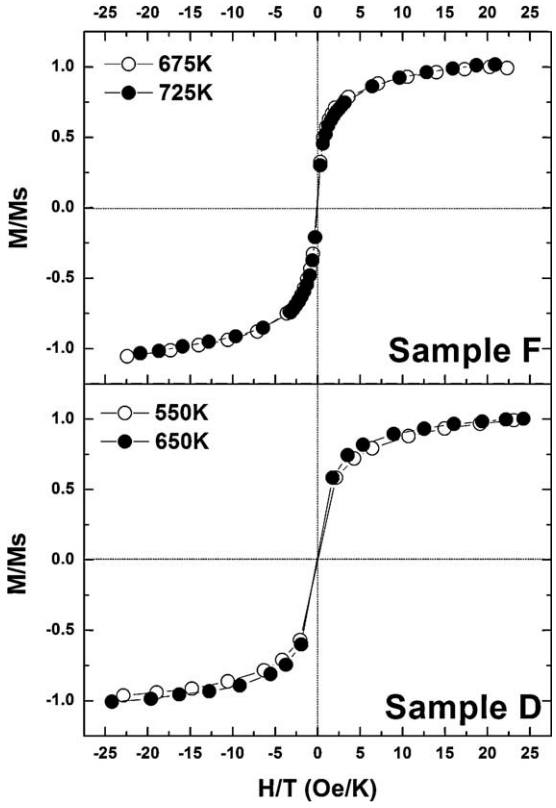

Fig. 17. M/M_s versus H/T curves for temperatures between T_B and superparamagnetic–paramagnetic transition phase temperature for sample D: nano-powder annealing at 500 °C and sample F: nano-powder sintering by SPS at 500 °C.

measurements as we did not use any precaution to avoid their interactions as we wanted to be able to compare the magnetization of nanoparticles to that of the corresponding compacted material. In fact, in our case for temperature below 300 K, saturation magnetization values calculated from hysteresis cycles are constant within error bars (Fig. 16).

In conclusion, according to Tronc et al.,[53] the SP systems studied here present a modified superparamagnetic regime mainly due to aggregation and dipolar interactions between nanoparticles. Furthermore, the blocking temperature increases with the size of the (see Table 3), in good agreement with the Dormann relation.[54] It reaches value significantly higher than room temperature (550 K). To the best of our knowledge, only one work recently reported on calcinated Ni-Zn ferrite nanoparticles with a probable blocking temperature higher than 330 K (temperature not measured).[44] Finally, in order to confirm the superparamagnetic behavior, we performed hysteresis cycles also for T above blocking temperature and below the Curie temperature where magnetization starts to be negligible. Due to the fact that the range between T_{diff} and T_C is narrow, the measurements were only conducted at two temperatures for each sample. For all SP samples, M/M_s versus H/T curves almost coincide in a universal curve so confirming the superparamagnetic behavior for all our samples[54,55] (we show as an example in Fig. 17 results obtained for the nanopowder heated at 500 °C – sample C – and the corresponding SPS sintered bulk at 500 °C – sample F).

Processing nanostructured spinel with a superparamagnetic character and a blocking temperature significantly higher than room temperature, has been possible in this work thanks to SPS which appears the most powerful sintering technique allowing consolidation of nanopowders into engineering components with limited growth of nanoparticles. This leads to bulk nanostructured material whose physical properties are close to those of the as-started nanoparticles (here superparamagnetism).

4. Conclusion

In this work we combined soft chemistry synthesis of nanoparticles and unusual compaction methods namely SPS and HIP to nanostructure spinel $CoFe_2O_4$ ceramics. The SPS method allowed us to produce bulk nanostructured materials with relative density about 92% in which nanoparticles maintain their size. Furthermore, the nanoparticles appear to be monocristalline since their size coincides, within the experimental error, with that of crystallite. On the contrary, HIP consolidation leads to polycrystalline micrometric particles (0.2–2 μm) while the nanopowder particles before consolidation are nanometric. We also observed that the mechanical hardness of the nanostructured bulk materials increases linearly with the sintering temperature. For the first time to our knowledge, it was possible to drive the hardness of the consolidated samples from that type of ductile metal to that type of ceramic such as spinel $MgAl_2O_4$ and this simply by controlling the SPS consolidation temperature. Another remarkable result here reported is that nanostructured bulk SPS sintered samples present superparamagnetic behavior evidenced by a blocking temperature. This critical temperature increases when the particle size increases. A critical temperature significantly higher than room temperature can be reached by simply controlling the sintering parameters. Furthermore, all the consolidated materials present a high magnetization saturation approaching that of the corresponding bulk spinel. In order to get more insight into the magnetic behavior of our systems, complementary magnetic studies are currently in progress and will be presented in another work focusing on magnetic properties. To conclude all these magnetic properties along with the tunable hardness open such materials for several promising applications.

Acknowledgments

This work has been supported by the "Région Île-de-France" in the framework of ECO-NANO project sponsored by C'Nano IdF. C'Nano IdF is the nanoscience competence center of Paris region, supported by CNRS, CEA, MESR and Region Ile-de-France. We also thank O. Rouleau and B. Villeroy from "Institut de Chimie et des Matériaux Paris-Est - UMR 7182" for letting us performing the magnetic measurements and SPS sintering.We are indebted to Dr. D. Foriani from CNRS Roma, Italy and to Dr. R.F. Jardim from University of São Paulo, Brazil for their advices and suggestions allowing us to give, in the revised version, more deeper analysis of the magnetic properties.

Special thanks to J. Morrice-Abrioux (IUT Saint-Denis, Université Paris 13) for careful reading of the final version.

References

1. Gleiter H. Nanostructured materials: basic concepts and microstructure. *Acta Mater* 2000;**48**:1–29.
2. Zhu YT, Lowe TC, Langdon TG. Performance and applications of nanostructured materials produced by severe plastic deformation. *Scripta Mater* 2004;**51**:825–30.
3. Valiev RZ, Islamgaliev RK, Alexandrov IV. Bulk nanostructured materials from severe plastic deformation. *Prog Mater Sci* 2000;**45**:103–89.
4. Moyet RP, Cardona Y, Vargas P, Silva J, Uwakweh ONC. Coercivity and superparamagnetic evolution of high energy ball milled (HEBM) bulk $CoFe_2O_4$ material. *Mater Char* 2010;**61**:1317–25.
5. Erb U. Electrodeposited nanocrystals: synthesis, properties and industrial applications. *Nanostruct Mater* 1995;**6**:533–8.
6. Kodama RH. Magnetic nanoparticles. *J Magn Magn Mater* 1999;**200**:359–72.
7. Kumar D, Gupta A. Evolution of structural and magnetic properties of sputtered nanocrystalline Co thin films with thermal annealing. *J Magn Magn Mater* 2007;**308**:318–24.
8. Chaim R. Densification mechanisms in spark plasma sintering of nanocrystalline ceramics. *Mater Sci Eng A* 2007;**443**:25–32.
9. Millot N, Le Gallet S, Aymes D, Bernard F, Grin Y. Spark plasma sintering of cobalt ferrite nanopowders prepared by coprecipitation and hydrothermal synthesis. *J Eur Ceram Soc* 2007;**27**:921–6.
10. Pileni MP, Moumen N, Hochepied JF, Bonville P, Veillet P. Control of the size of cobalt ferrite nanoparticles: synthesis and properties. *J Phys IV* 1997;**7**:505–8.
11. Kim YI, Kim D, Lee CS. Synthesis and characterization of $CoFe_2O_4$ magnetic nanoparticles prepared by temperature-controlled coprecipitation method. *Physica B* 2003;**337**:42–51.
12. Chinnasamy CN, Senoue M, Jeyadevan B, Perales-Perez O, Shinoda K, Tohji K. Synthesis of size-controlled cobalt ferrite particles with high coercivity and squareness ratio. *J Colloid Interface Sci* 2003;**263**:80–3.
13. Qu YQ, Yang HB, Yang N, Fan YZ, Zhu HY, Zou GT. The effect of reaction temperature on the particle size, structure and magnetic properties of coprecipitated $CoFe_2O_4$ nanoparticles. *Mater Lett* 2006;**60**:3548–52.
14. Baldi G, Bonacchi D, Innocenti C, Lorenzi G, Sangregorio C. Cobalt ferrite nanoparticles: the control of the particle size and surface state and their effects on magnetic properties. *J Magn Magn Mater* 2007;**311**:10–6.
15. Kumar V, Rana A, Yadav MS, Pant RP. Size-induced effect on nanocrystalline $CoFe_2O_4$. *J Magn Magn Mater* 2008;**320**:1729–34.
16. Chia CH, Zakaria S, Yusoff M, Goh SC, Haw CY, Ahmadi S, et al. Size and crystallinity-dependent magnetic properties of $CoFe_2O_4$ nanocrystals. *Ceram Int* 2010;**36**:605–9.
17. Ammar S, Helfen A, Jouini N, Fievet F, Rosenman I, Villain F, et al. Magnetic properties of ultrafine cobalt ferrite particles synthesized by hydrolysis in a polyol medium. *J Mater Chem* 2001;**11**:186–92.
18. Giri AK, Pellerin K, Pongsaksawad W, Sorescu M, Majetich SA. Effect of light on the magnetic properties of cobalt ferrite nanoparticles. *IEEE Trans Magn* 2000;**36**:3029–31.
19. Giri AK, Kirkpatrick EM, Moongkhamklang P, Majetich SA, Harris VG. Photomagnetism and structure in cobalt ferrite nanoparticles. *Appl Phys Lett* 2002;**80**:2341–3.
20. Cabuil V, Dupuis V, Talbot D, Neveu S. Ionic magnetic fluid based on cobalt ferrite nanoparticles: influence of hydrothermal treatment on the nanoparticle size. *J Magn Magn Mater* 2011;**323**:1238–41.
21. Poul L, Jouini N, Fievet F. Layered hydroxide metal acetates (metal = zinc, cobalt, and nickel): elaboration via hydrolysis in polyol medium and comparative study. *Chem Mater* 2000;**12**:3123–32.
22. Poul L, Ammar S, Jouini N, Fievet F, Villain F. Synthesis of inorganic compounds (metal, oxide and hydroxide) in polyol medium: a versatile route related to the sol–gel process. *J Sol–Gel Sci Technol* 2003;**26**:261–5.
23. Kellett BJ, Lange FF. Experiments on pore closure during hot isostatic pressing and forging. *J Am Ceram Soc* 1988;**71**:7–12.
24. Tressler RE, Langensira Bradt RC. Surface-finish effects on strength-vs-grain-size relations in polycrystalline Al_2O_3. *J Am Ceram Soc* 1974;**57**:226–7.
25. Rizkallah C, Fondere JP, Raynaud HF, Vignes A. Advanced process control of hot isostatic pressing application to Astroloy HIP. *Rev Metall-Cahiers D Inform Tech* 2001;**98**:1109.
26. Rodriguez-Carvajal J. Recent advances in magnetic-structure determination by neutron powder diffraction. *Physica B* 1993;**192**:55–69.
27. Williamson GK, Hall WH. X-ray line broadening from filed aluminum and wolfram. *Acta Metall* 1953;**1**:22–31.
28. Caglioti G, Paoletti A, Ricci FP. Choice of collimators for a crystal spectrometer for neutron diffraction. *Nucl Instrum Methods* 1958;**3**:223–8.
29. Poix P. Liaisons interatomiques et propriétés physiques des composés minéraux. *Seminaire Etat Solide* 1966–1967;**1**:82–119.
30. Poix P, Basile F, Djega-Mariadassou C. Etude de la variation du paramètre de maille en fonction de la distribution des actions dans les systèmes γFe_3O_4, $(1-\gamma)FeCr_2O_4$ et γFe_3O_4, $(1-\gamma)FeSnO_4$. *Ann Chim* 1975;**3**:159–62.
31. Dakhlaoui A, Jendoubi M, Smiri LS, Kanaev A, Jouini N. Synthesis, characterization and optical properties of ZnO nanoparticles with controlled size and morphology. *J Cryst Growth* 2009;**311**:3989–96.
32. Dakhlaoui A, Smiri LS, Babadjian G, Schoenstein F, Molinie P, Jouini N. Controlled elaboration and magnetic properties of submicrometric cobalt fibers. *J Phys Chem C* 2008;**112**:14348–54.
33. Liu XM, Zhou YC. Seed-mediated synthesis of uniform ZnO nanorods in the presence of polyethylene glycol. *J Cryst Growth* 2004;**270**:527–34.
34. George M, John AM, Nair SS, Joy PA, Anantharaman MR. Finite size effects on the structural and magnetic properties of sol–gel synthesized $NiFe_2O_4$ powders. *J Magn Magn Mater* 2006;**302**:190–5.
35. Liu BW, Zhang Y. $La_{0.9}Sr_{0.1}Ga_{0.8}Mg_{0.2}O_{3-\delta}$ sintered by spark plasma sintering (SPS) for intermediate temperature SOFC electrolyte. *J Alloys Compd* 2008;**458**:383–9.
36. Kodash VY, Groza JR, Cho KC, Klotz BR, Dowding RJ. Field-assisted sintering of Ni nanopowders. *Mater Sci Eng A* 2004;**385**:367–71.
37. Groza JR, Dowding RJ. Nanoparticulate materials densification. *Nanostruct Mater* 1996;**7**:749–68.
38. Qiao J, Xi Z, Tang H, Wang J, Zhu J. Influence of porosity on quasi-static compressive properties of porous metal media fabricated by stainless steel fibers. *Mater Design* 2009;**30**:2737–40.
39. Bate G. *Ferromagnetic materials*, vol. 2. North-Holland, Amsterdam: E P Wohlfarth; 1980.
40. Malats I. Riera A, Pourroy G, Poix P. Syncrystallization of $CoFe_2O_4$ from ferric and cobaltous chlorides – physical properties of the precipitate. *J Solid State Chem* 1992;**101**:195–8.
41. Chinnasamy CN, Jeyadevan B, Shinoda K, Tohji K, Djayaprawira DJ, Takahashi M, et al. Unusually high coercivity and critical single-domain size of nearly monodispersed $CoFe_2O_4$ nanoparticles. *Appl Phys Lett* 2003;**83**:2862–4.
42. Arcos D, Vallet-Regi M. Improved mechanical properties in Nb_2O_5/V_2O_5 doped spinel ferrites. *J Solid State Chem* 1999;**148**:376–9.
43. Bhaduri S, Bhaduri SB. Microstructural and mechanical properties of nanocrystalline spinel and related composites. *Ceram Int* 2002;**28**:153–8.
44. Beji Z, Smiri LS, Yaacoub N, Grenèche JM, Menguy N, Ammar S, et al. Annealing effect on the magnetic properties of polyol-made Ni-Zn ferrite nanoparticles. *Chem Mater* 2010;**22**:1350–66.
45. Wei W, Egilmez M, Chen W, Jung J, Ivey D. Strong correlation between the cation ordering and magnetic properties of anodically electrodeposited Mn-Co-O nanocrystals. *J Mater Sci* 2010;**45**:6824–9.
46. Markovich V, Jung G, Fita I, Mogilyansky D, Wu X, Wisniewski A, et al. Magnetotransport properties of ferromagnetic $LaMnO_{3+\delta}$ nano-sized crystals. *J Magn Magn Mater* 2010;**322**:1311–4.
47. Paulsen JA, Lo CCH, Snyder JE, Ring AP, Jones LL, Jiles DC. Study of the Curie temperature of cobalt ferrite based composites for stress sensor applications. *IEEE Trans Magn* 2003;**39**:3316–8.
48. Franco JA, e Silva FC. High temperature magnetic properties of cobalt ferrite nanoparticles. *Appl Phys Lett* 2010;**96**:172505–11.
49. Mazumdar C, Nagarajan R, Gupta LC, Padalia BD, Vijayaraghavan R. SmNi4B: a narrow domain-wall ferromagnet. *Appl Phys Lett* 2000;**77**:895–7.

50. Manova E, Kunev B, Paneva D, Mitov I, Petrov L, Estournes C, et al. Mechano-synthesis, characterization, and magnetic properties of nanoparticles of cobalt ferrite, $CoFe_2O_4$. *Chem Mater* 2004;**16**:5689–96.
51. Makhlouf SA, Parker FT, Berkowitz AE. Magnetic hysteresis anomalies in ferritin. *Phys Rev B* 1997;**55**:14717–20.
52. Walmsley NS, Chantrell RW, Gore JG, Maylin M. Experimental and computational investigation of the magnetic susceptibility of composite soft materials. *J Phys D* 2000;**33**:784–90.
53. Tronc E, Prené P, Jolivet JP, Fiorani D, Testa AM, Cherkaoui R, et al. Magnetic dynamics of γ-Fe_2O_3 nanoparticles. *Nanostruct Mater* 1995;**6**:945–8.
54. Dormann JL. Superparamagnetism phenomenon. *Rev Phys Appl* 1981;**16**:275–301.
55. Grigorova M, Blythe HJ, Blaskov V, Rusanov V, Petkov V, Masheva V, et al. Magnetic properties and Mossbauer spectra of nanosized $CoFe_2O_4$ powders. *J Magn Magn Mater* 1998;**183**:163–72.